Electronic Supplementary Information

Dynamic Self-assembly of Small Molecules Enables Spontaneous Fabrication of Hole Conductor at Perovskite/electrode Interfaces for over 22% Stable Inverted Perovskite Solar Cells

Wanhai Wang,‡[a,b] Kun Wei,‡[a] Li Yang,[a] Jidong Deng,[a] Jinbao Zhang[a,c] and Weihua Tang*[a,b]*

[a] Institute of Flexible Electronics (IFE, Future Technologies), College of Materials, Fujian Key Laboratory of Advanced Materials, Xiamen Key Laboratory of Electronic Ceramic Materials and Devices, Innovation Laboratory for Sciences and Technologies of Energy Materials of Fujian Province (IKKEM), Xiamen University, Xiamen, 361005, China.
E-mail: whtang@xmu.edu.cn.

[b] School of Chemistry and Chemical Engineering, Nanjing University of Science and Technology, Nanjing 210094, P. R. China.

[c] Shenzhen Research Institute of Xiamen University, Shenzhen, 518000, P. R. China.
E-mail: jinbao.zhang@xmu.edu.cn.

‡These authors contributed equally to the work.

1. Experimental details

1.1. Materials and device structures

Lead (II) iodide (PbI_2) and Lead (II) bromide ($PbBr_2$) were purchased from TCI (Japan). Cesium iodide (CsI), methylammonium chloride (MACl), formamidinium bromide (FABr), and C60 were purchased from Xi'an Polymer Light Technology Corp (China). Formamidinium iodide (FAI), methylammonium iodide (MAI), bathocuproine (BCP), Indium tin oxide glass (ITO) substrate were purchased from Advanced electron technology CO, Ltd (China). Toluene, chlorobenzene (CB), isopropanol (IPA), N,N-dimethylformamide (DMF), dimethyl sulfoxide (DMSO), and ethyl acetate (EA) were purchased from Sigma-Aldrich (USA).

The synthesis of BCB-C4PA is depicted in **Scheme S1**. A three-step reaction route including alkylation with dibromobutane, Arbuzov reaction to introduce phosphonic acid ester group, and cleavage of the ethyl groups with bromotrimethylsilane are performed in sequence to generate the compound BCB-C4Br, BCB-C4P and BCB-C4PA, respectively. The reference SAM, i.e., CZ-C4PA, was prepared by following the similar approach as reported in the literature.[1,2] Structures of the synthesized compounds were confirmed by means of ^{1}H, ^{13}C nuclear magnetic resonance spectroscopy (NMR) and matrix-assisted laser desorption/ionization time-of-flight (MALDI-TOF) mass spectra. The detailed synthetic procedures are listed as below.

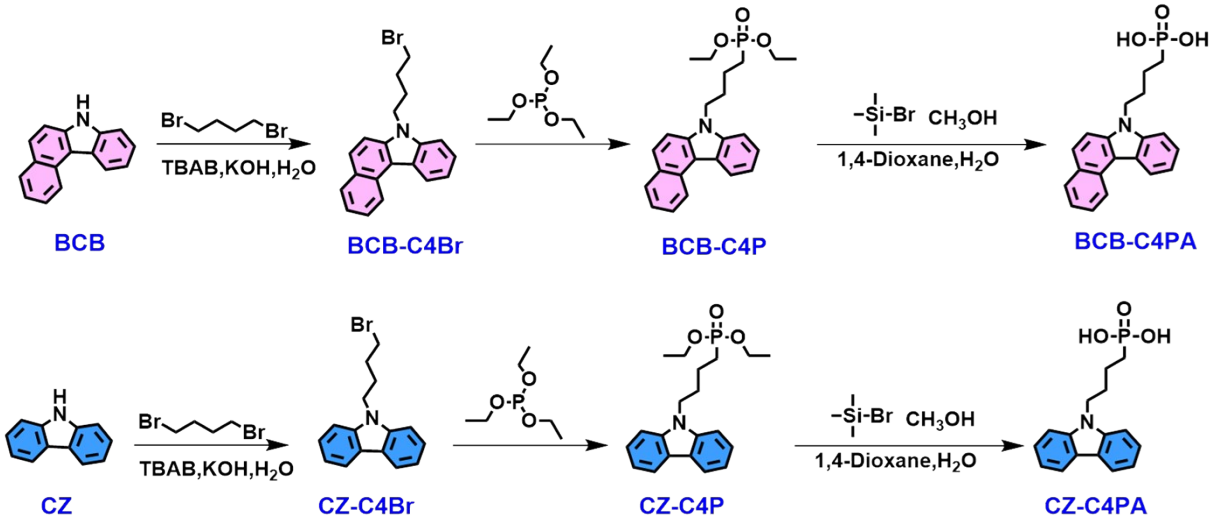

Scheme S1. Synthetic routes of **BCB-C4PA** and **CZ-C4PA**.

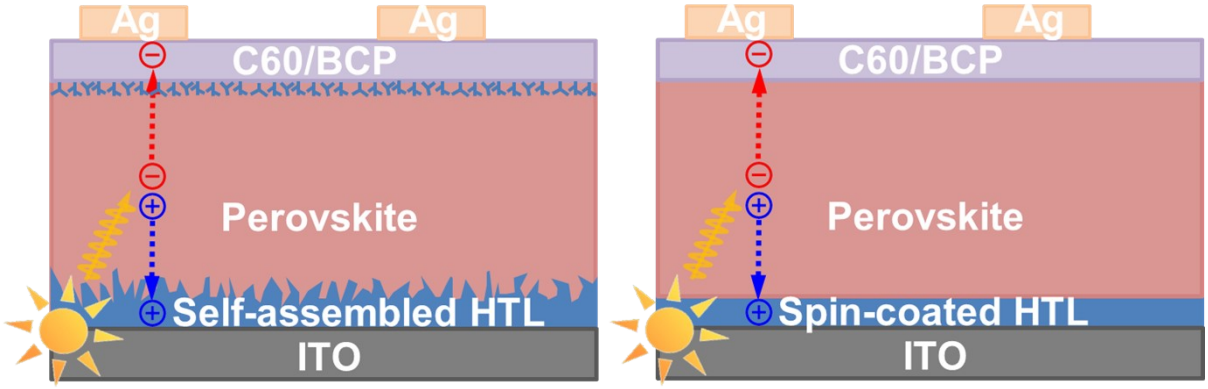

Scheme S2. Schematic of the p-i-n device architecture using ISSA strategy (left) and independent spin-coating method (right).

1.2 Instruments and general methods

The ^{1}H and ^{13}C NMR spectra were measured in deuterated chloroform ($CDCl_3$) or dimethyl sulfoxide (DMSO-*d*6) solvent using Bruker AVANCE 500 MHz spectrometer with tetramethylsilane (TMS) as internal standard. The matrix assisted laser desorption/ionization time-of-flight (MALDI-TOF) mass spectra were recorded using a Bruker Autoflex TOF/TOF spectrometer.

Density Functional Theory (DFT) established in Gaussian09 code with the B3LYP/6-31G (d, p) basis set was used to conduct theoretical simulation and calculation of molecular conformation, energy level and surface electrostatic potential.[3] The molecular structures were optimized by Chem3D before being calculated by DFT. Then, the resulted files were further used to calculate electrostatic potential (ESP) by a software of Multiwfn. Then molecular electrostatic potential surfaces were mapped by a software of VMD with electron density of 0.001 e $Bohr^{-3}$.

Ultraviolet-visible absorption spectra were obtained using a UV-1900 spectrophotometer. Ultraviolet photoelectron spectroscopy (UPS) was performed by PHI 5000 VersaProbe III with He I source (21.22 eV) under an applied negative bias of 5.0 V. The thermogravimetric analysis (TGA) was tested using a TGA/SDTA851E (Mettler Toledo) with a heating rate of 20°C min^{-1} from 50 to 800°C under nitrogen gas flow. The TOF-SIMS results were gained by using a PHI nanoTOF II Time-of-Flight SIMS, in which Bi_3^+ (30 keV) was used to probe the sample surface in the analysis phase and Ar clusters (3 kV) were used in the sputtering at a sputter rate of 10nm/min.[4] The XRD pattern were measured by Bruker-axs XRD with a Cu Kα radiation source. The micro-morphology of films top and bottom surface was characterized by SEM (SU-70, Japan Hitachi Nake high-tech enterprise). The water contact angles of water on different sample surfaces were measured by using a video optical contact angle meter (Dataphysics, OCA20). The photographs were taken immediately after water dripping.

Exfoliation of the perovskite films: Before the blade coating, PMMA (0.4 g PMMA was dissolved in 1 mL CB) and epoxy (bisphenol A diglycidyl ether(2,2-bis[4-(glycidyloxy)phenyl]propane, 4,4′-isopropylidenedi-phenol diglycidyl ether), octylamine and m-xylylenediamine were mixed with a molar ratio of 4:2:1) precursor solution were prepared.[5] PMMA and epoxy layer were blade coated on the prepared perovskite film in a sequential order. In order to accelerate the cross-link process of epoxy, the coated substrate was annealed at 70 °C for 10 min. After 12 hours, the epoxy was completely solidified at room temperture. Finally, perovskite film was exfoliated from glass/ITO substrate by a glass nipping plier.

The *J-V* characteristics of PSCs were performed in a N_2 atmosphere under AM 1.5 G illumination using a Keithley 2400 Source Meter in combination with a Enlitech SS-X50 solar

simulator. EQE spectra were obtained using a solar cell spectral response measurement system QE-R (Enlitech Co., Ltd.). Mott-Schottky analysis was conducted by using electrochemical workstation (CHI 660) at a frequency of 1kHz with potential ranging from 0 V to 1.2 V. EIS and dark current analysis were measured by using electrochemical workstation (CHI 660) with a frequency range from 10 Hz to 100 kHz at an open circuit voltage in dark conditions. PL spectra were obtained by FLS1000 (Edinburgh instruments) with an excitation at 460 nm, and TRPL spectra were obtained by FLS1000 (Edinburgh instruments) with an excitation at 450 nm.

Capacitance–voltage measurement was conducted to study the interfacial electronic structures in devices:

$$\left(\frac{C}{A}\right)^2 = \frac{q\varepsilon\varepsilon_0 N}{2(V_{bi} - V)}$$

where V is the applied bias, A is the active area, e is the charge of the element, ε is the static permittivity of the perovskite, ε_0 is the vacuum permittivity, and N is the carrier concentration. The X-axis intersection represents the built-in potential V_{bi}, and the slope reflects the carrier density of the interface.[6]

2. Figures

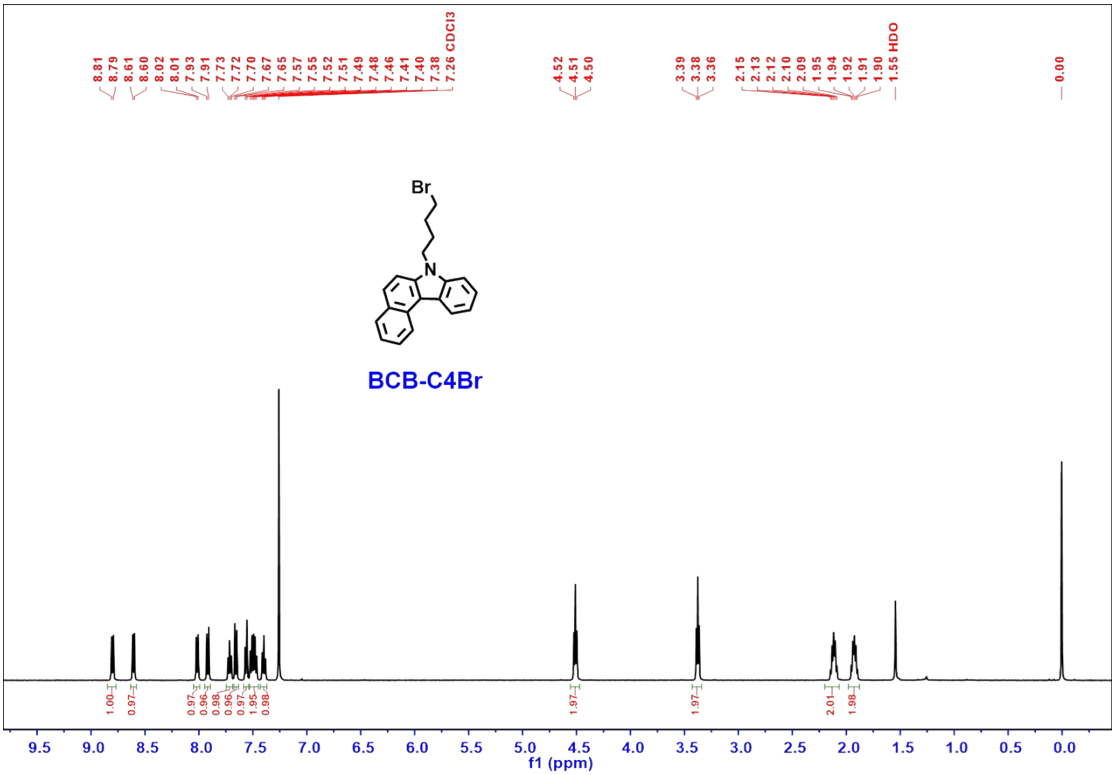

Fig. S1. ^{1}H NMR spectrum of **BCB-C4Br.**

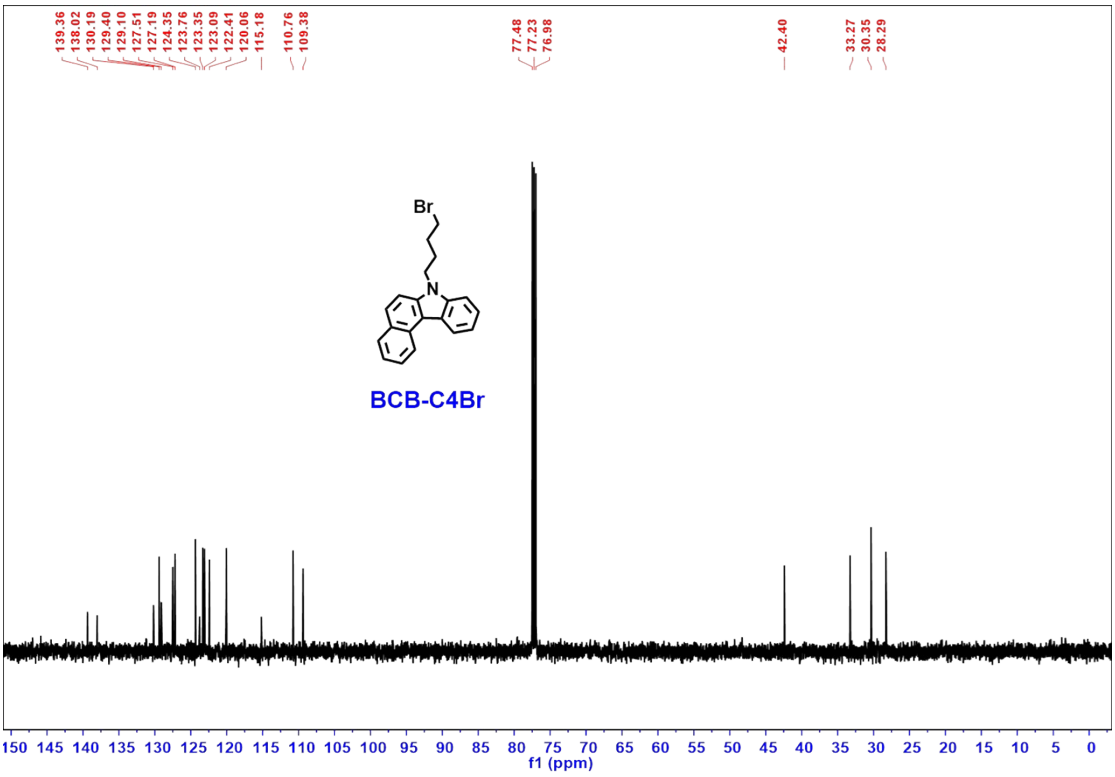

Fig. S2. ^{13}C NMR spectrum of **BCB-C4Br.**

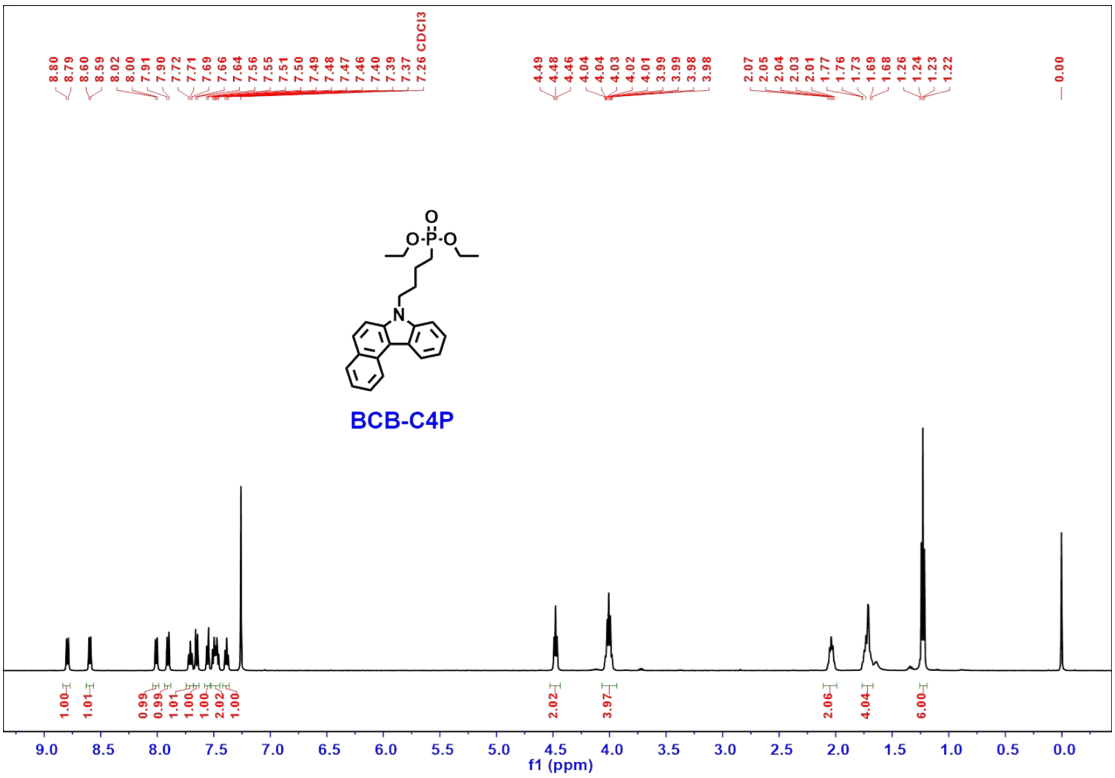

Fig. S3. ^{1}H NMR spectrum of **BCB-C4P.**

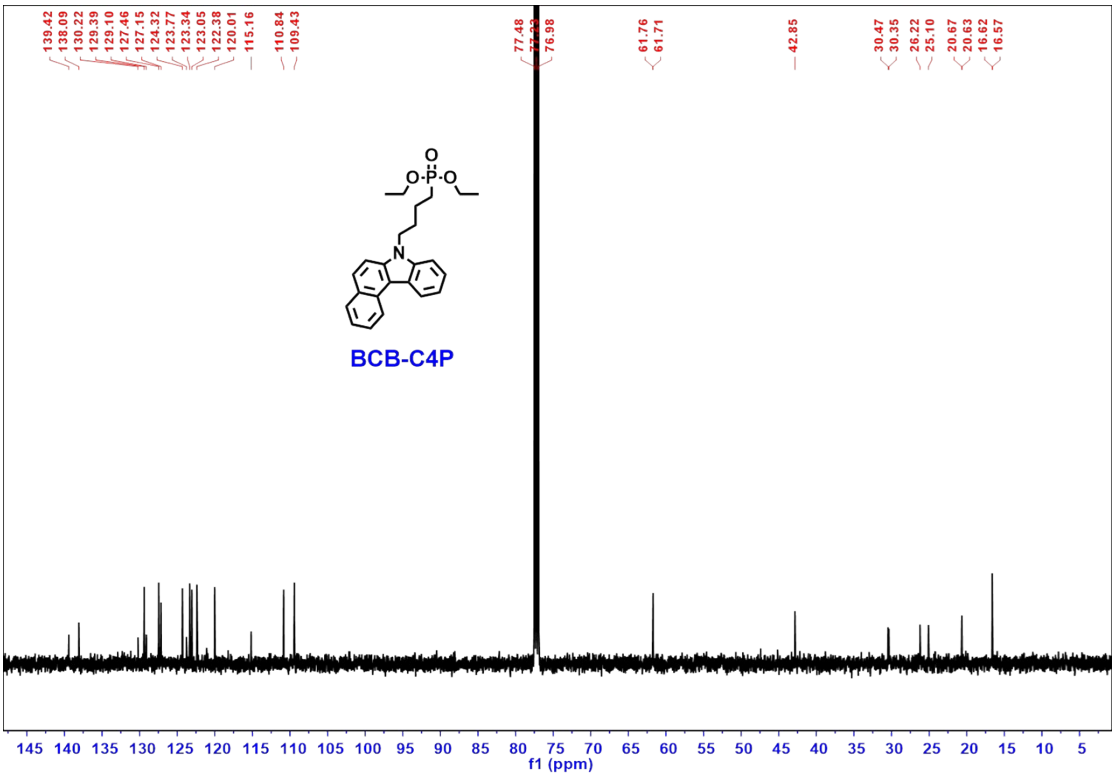

Fig. S4. ^{13}C NMR spectrum of **BCB-C4P.**

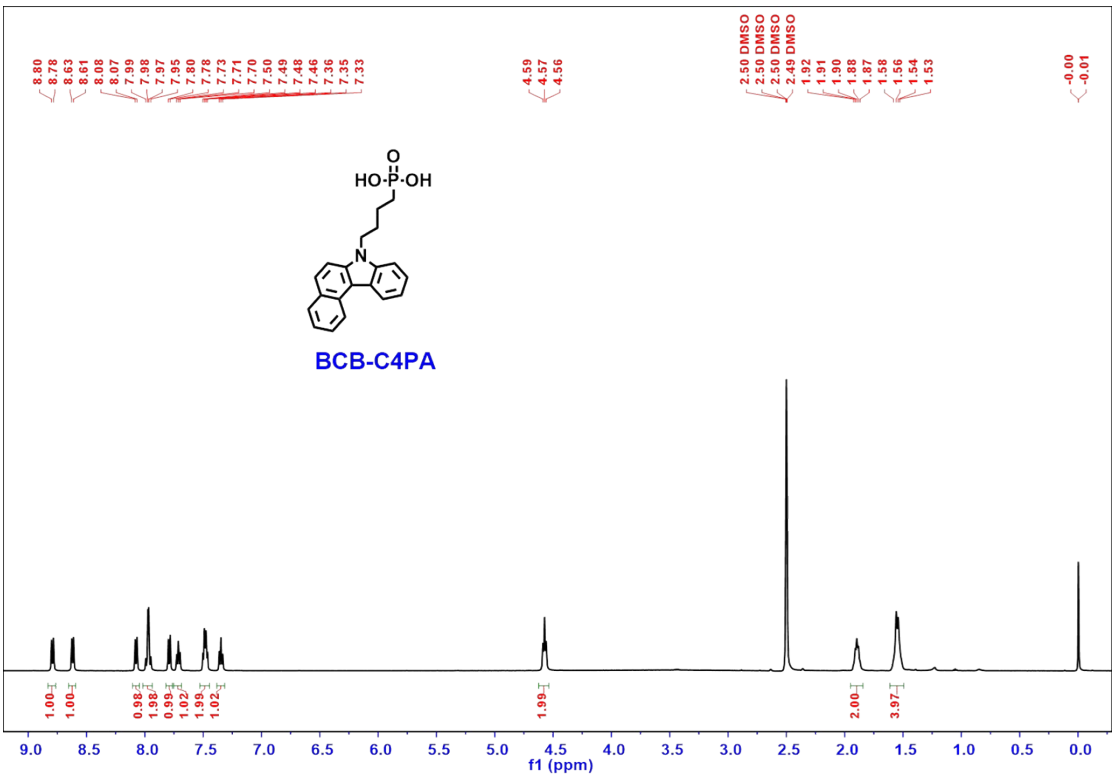

Fig. S5. ^{1}H NMR spectrum of **BCB-C4PA.**

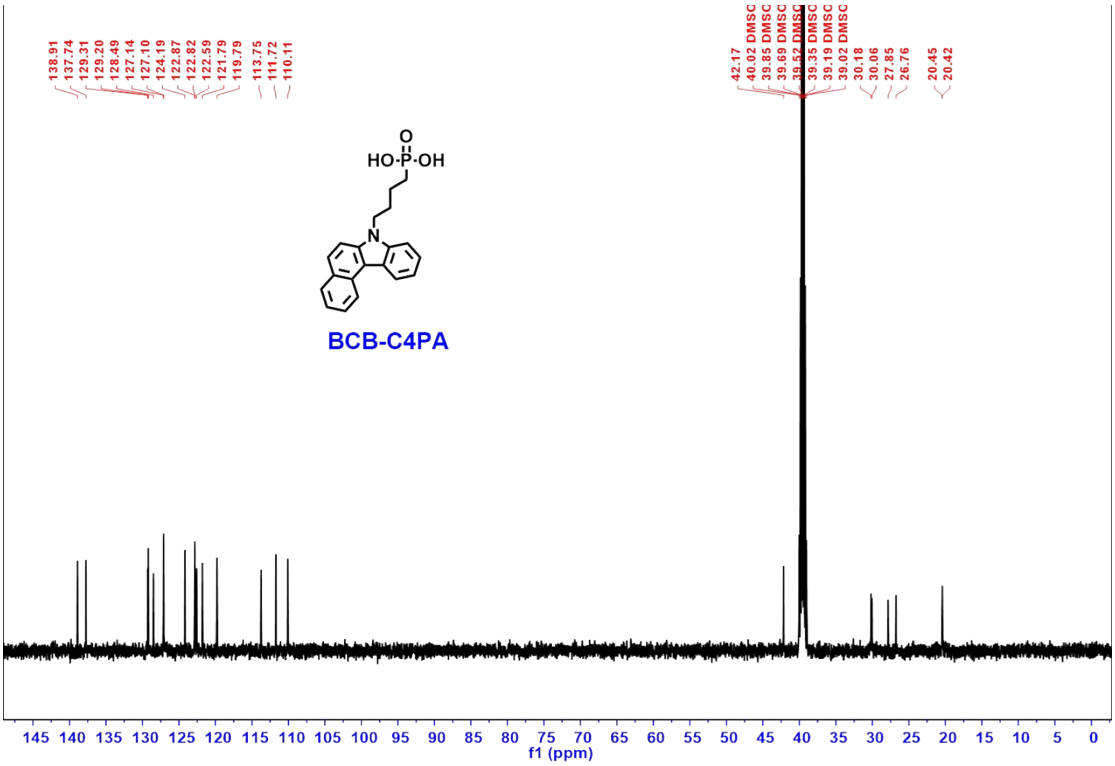

Fig. S6. ^{13}C NMR spectrum of **BCB-C4PA.**

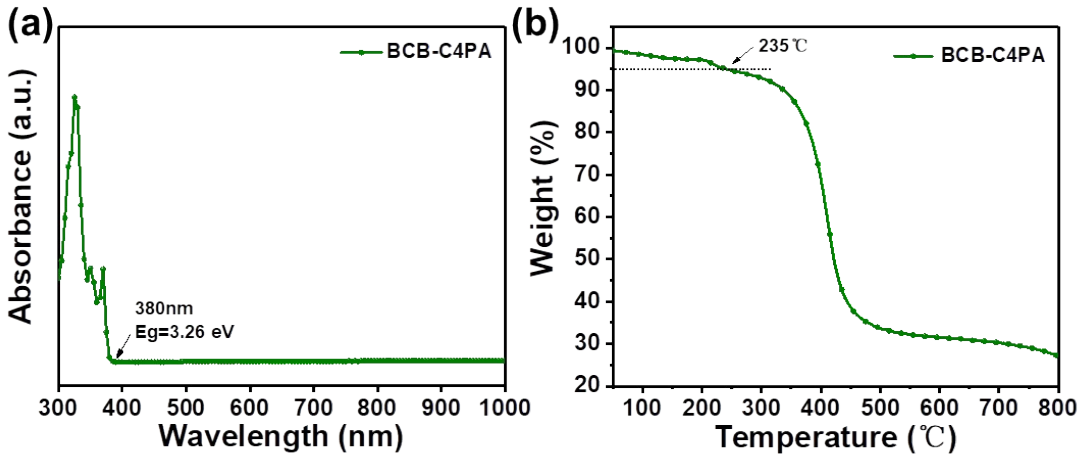

Fig. S7. Optical property and thermal stability of designed SAM. (a) UV-Vis absorption spectrum of BCB-C4PA in DMSO solution, from which its bandgap (E_g) is calcualted to be 3.26 eV. (b) Thermogravimetric analysis of BCB-C4PA with a heating rate of 20°C min^{-1} from 50 to 800°C under nitrogen gas flow.

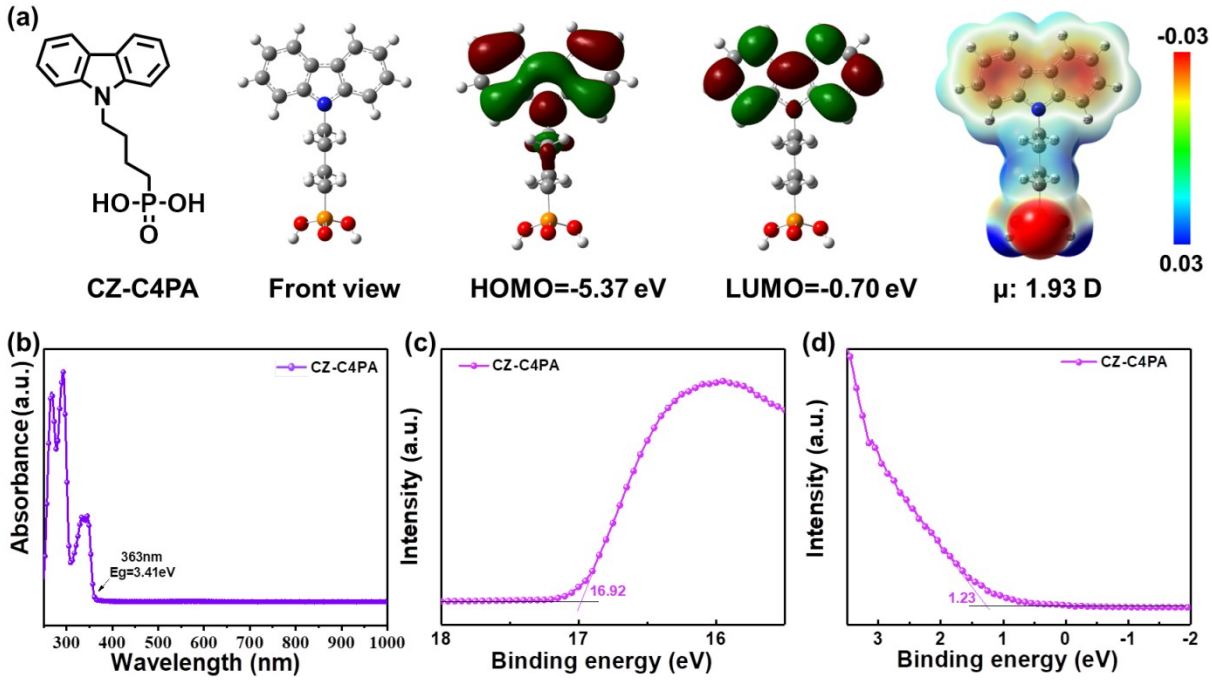

Fig. S8. Chemical structure and molecular properties of previously reported SAM. (a) Chemical structure and molecular simulation (including molecular geometry, frontier molecular orbital (FMO) energy levels, electrostatic potential surface (ESP) and dipole moment (μ)) of CZ-C4PA. (c) UV-vis absorbance spectra of CZ-C4PA in DMSO, from which an Eg of 3.41 eV can be estimated. (c) and (d) Ultra-violet photoelectron spectra (UPS) of CZ-C4PA spin-coated on ITO substrates (excitation energy is 21.22 eV).

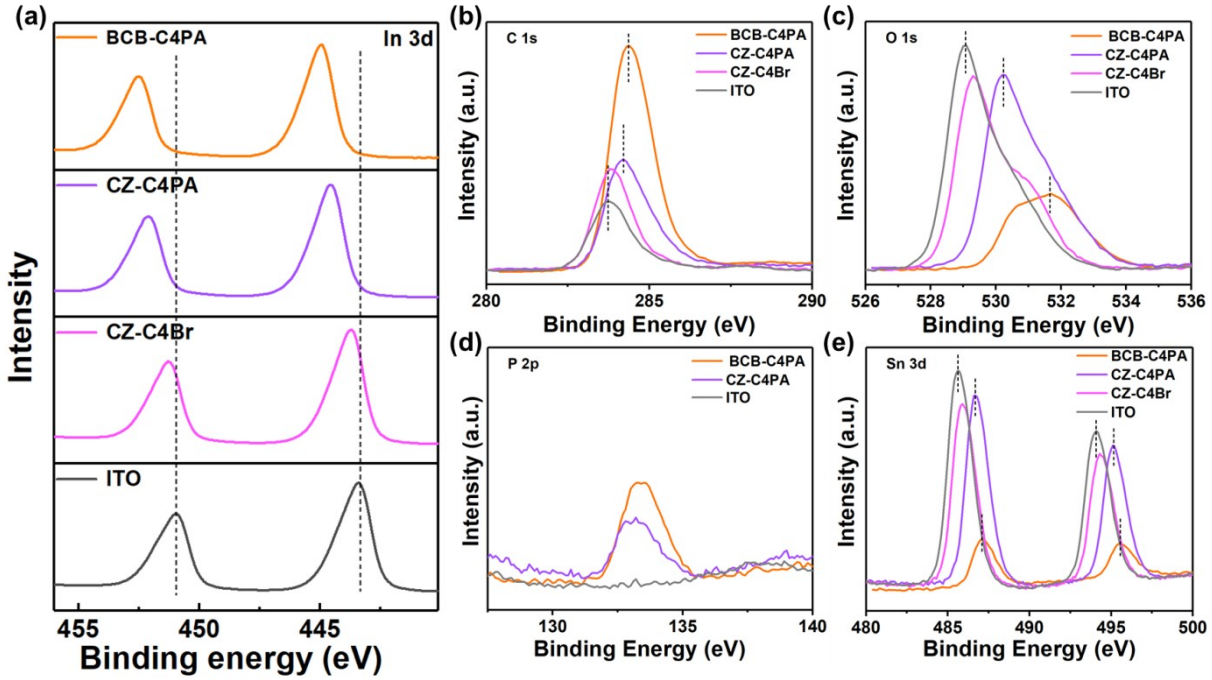

Fig. S9. X-ray spectroscopic characterizations of HTL-coated ITO substrates. X-ray photoelectron spectroscopy (XPS) spectra of the (a) In 3d, (b) C1s, (c) O1s, (d) P 2p and (e) Sn 3d binding energy regions of bare and HTL-coated ITO substrates. The dotted lines show the the peak shifts after spin-coating respective HTLs.

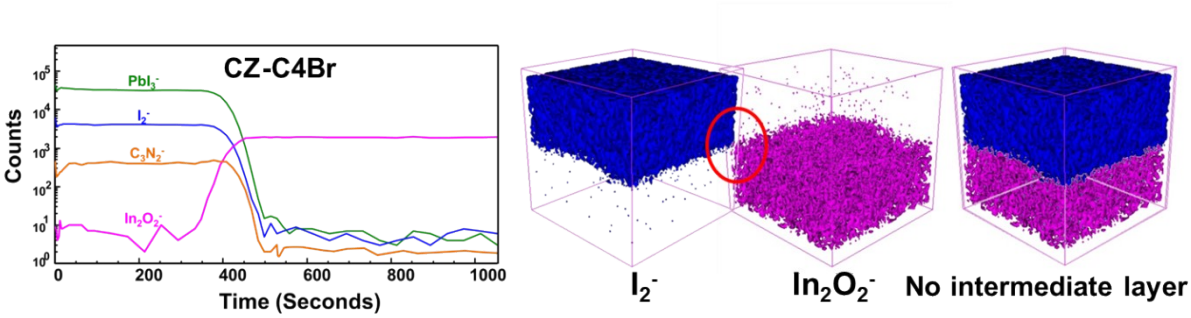

Fig. S10. The space distribution of blended CZ-C4Br using ISSA strtegy. Cross-section TOF-SIMS profiles (left) and corresponding 3D distribution pictures (right) of perovskite films prepared by ISSA strtegy using CZ-C4Br. Due to the low concentration of CZ-C4Br after dispersing in perovskite film, the signal (302 g mol^{-1}) indicating its distribution was not detected and no intermediate layer existed between the perovskite layer and the ITO substrate.

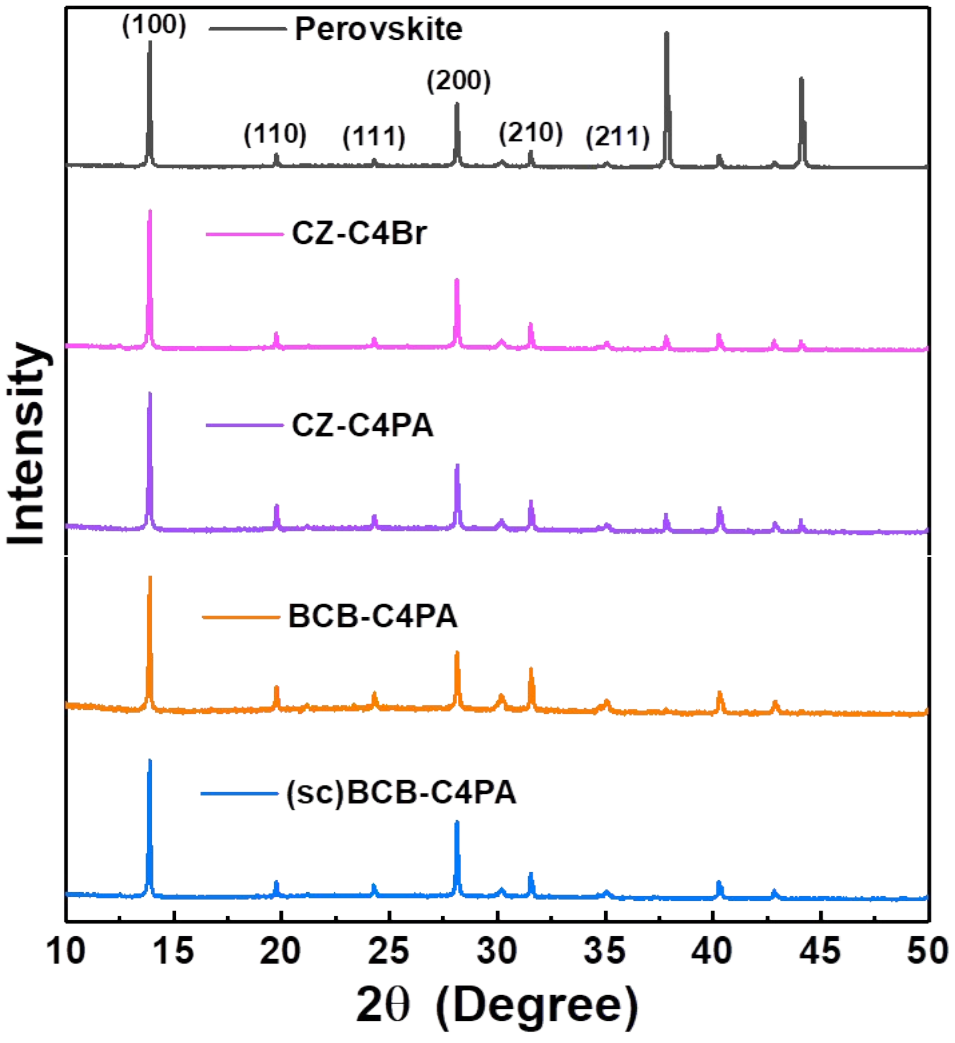

Fig. S11. X-ray diffractograms of CsMAFA perovskite films grown with in-situ blended BCB-C4PA, CZ-C4PA, CZ-C4Br or independently spin-coated BCB-C4PA.

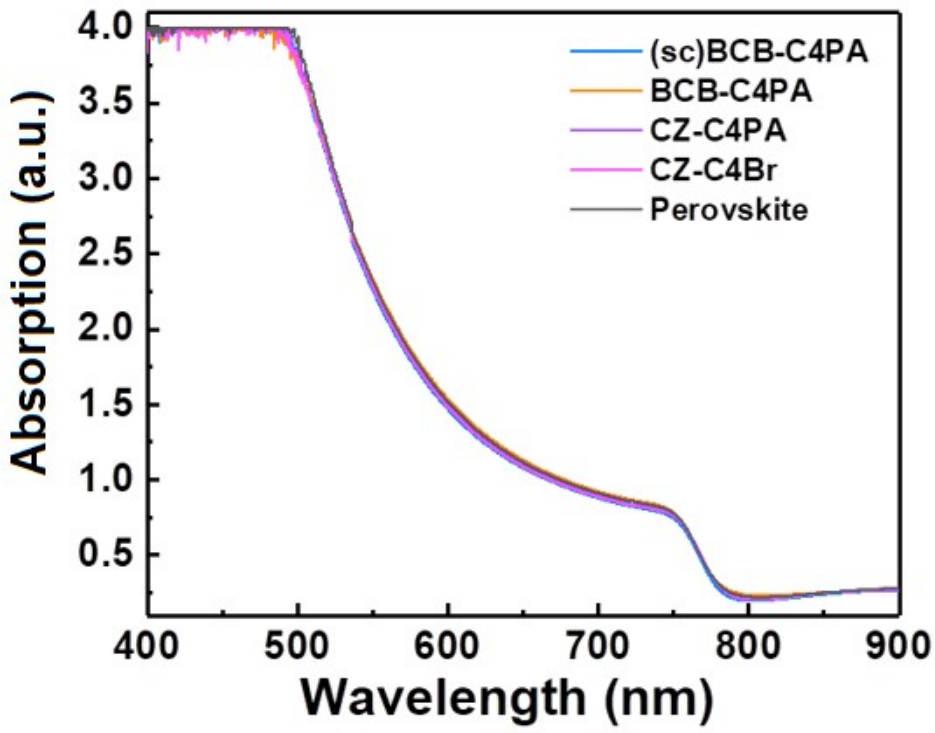

Fig. S12. UV-Vis absorption spectra of perovskite films prepared with or without respective HTLs .

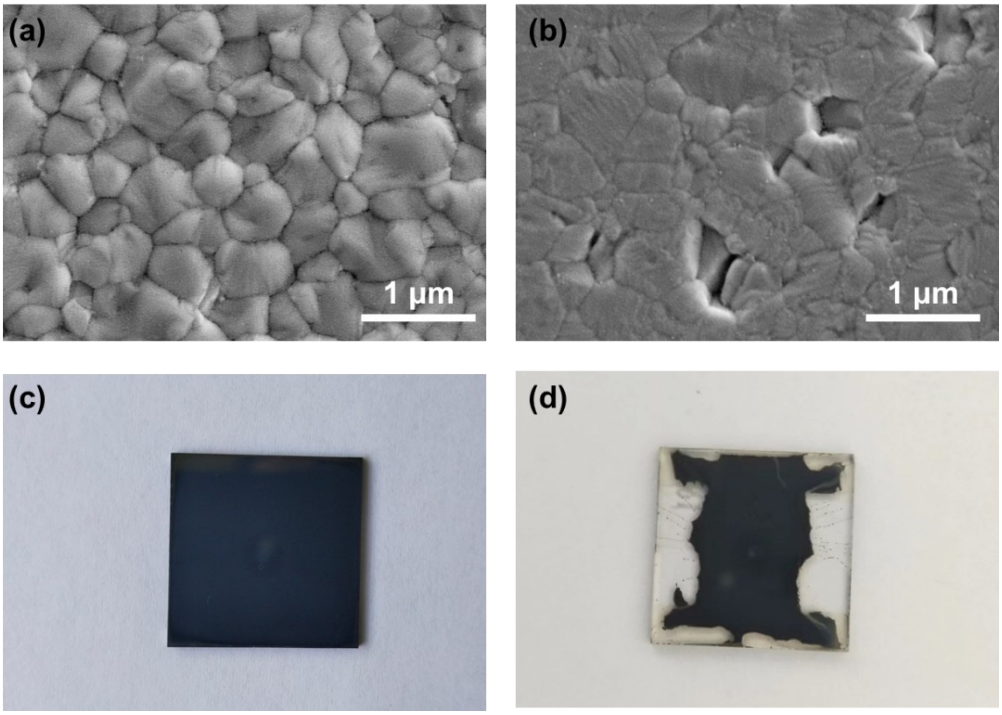

Fig. S13. The interfacial morphologies of pure perovskite films coated on ITO and the visual pictures of perovskite films prepared by differernt methods. SEM images of (a) top and (b) buried interfacs of pure perovskite spin-coated on ITO substrate. Visual pictures of perovskite films prepared by (c) *in-situ* blended BCB-C4PA and (d) independently spin-coated BCB-C4PA.

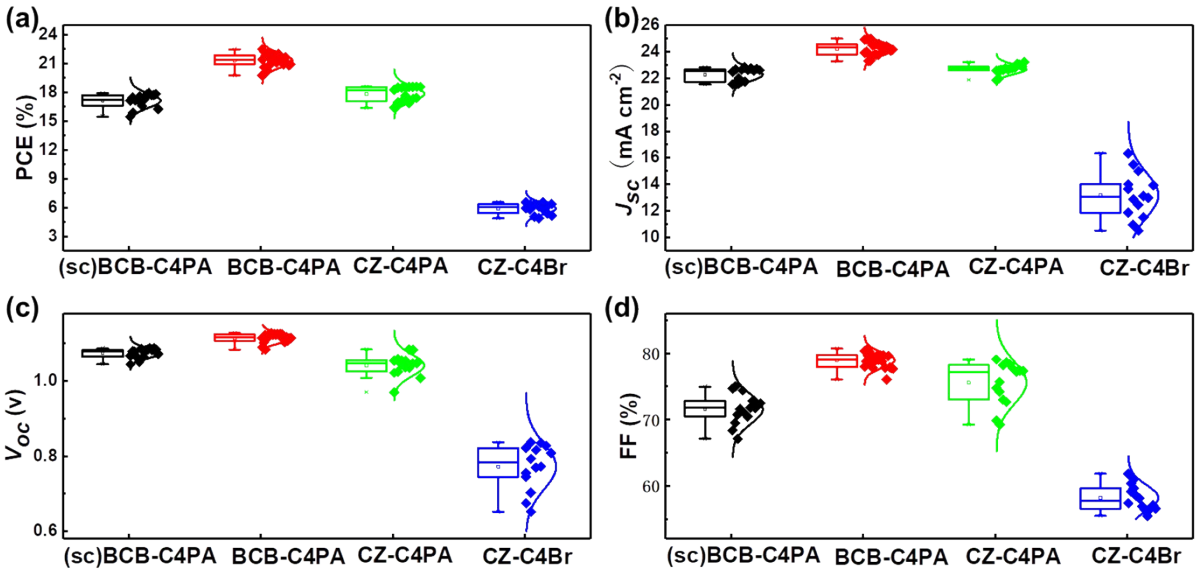

Fig. S14. The photovoltaic parameters (PCE, J_{SC}, V_{OC}, and FF) of optimized solar cells perpared by *in-situ* blended BCB-C4PA,CZ-C4PA, CZ-C4Br and independently spin-coated BCB-C4PA.

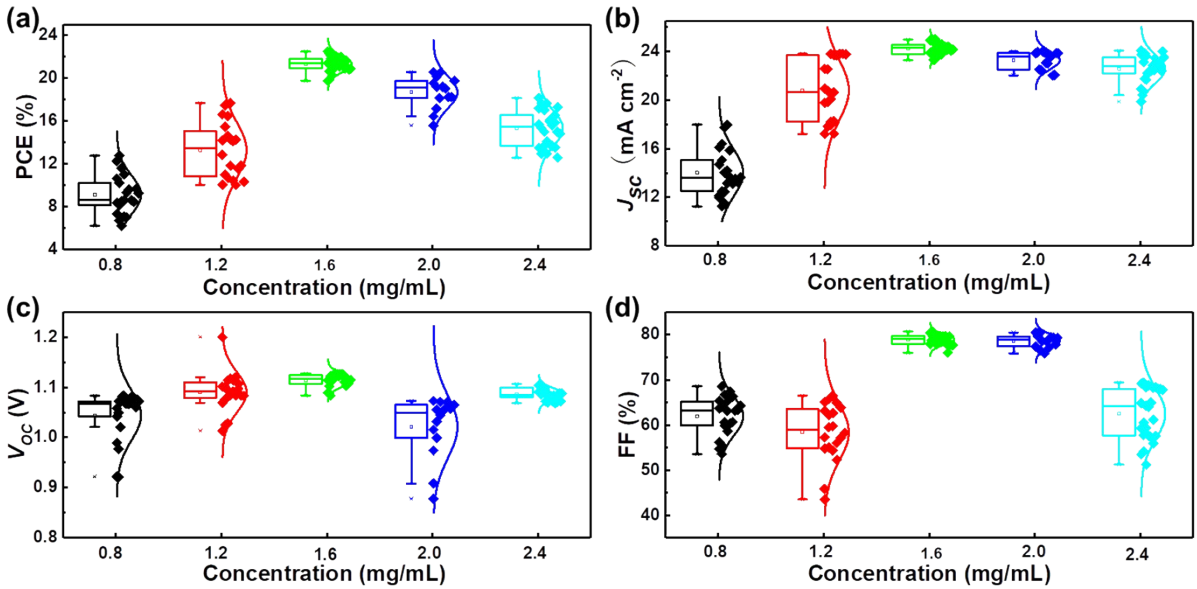

Fig. S15. Box plots of PCE, J_{SC}, V_{OC}, and FF values for solar cells perpared by *in-situ* blended BCB-C4PA under different concentrations.

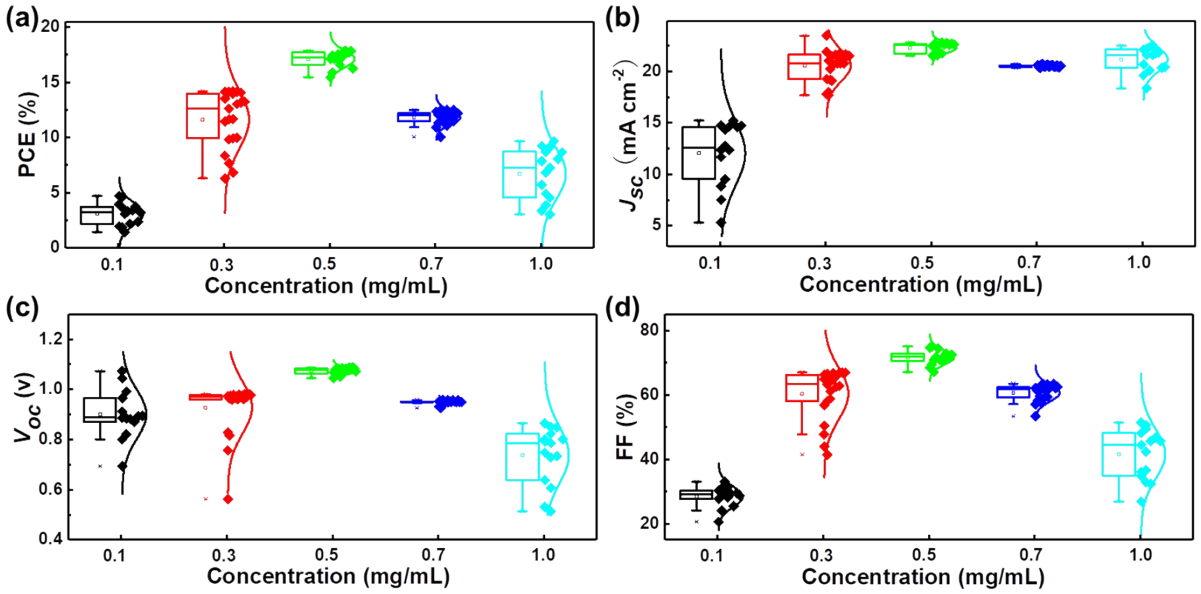

Fig. S16. Box plots of PCE, J_{SC}, V_{OC}, and FF values for solar cells perpared by independently spin-coated BCB-C4PA under different concentrations (BCB-C4PA is dissolved in ethanol and spin-coated on ITO substrate).

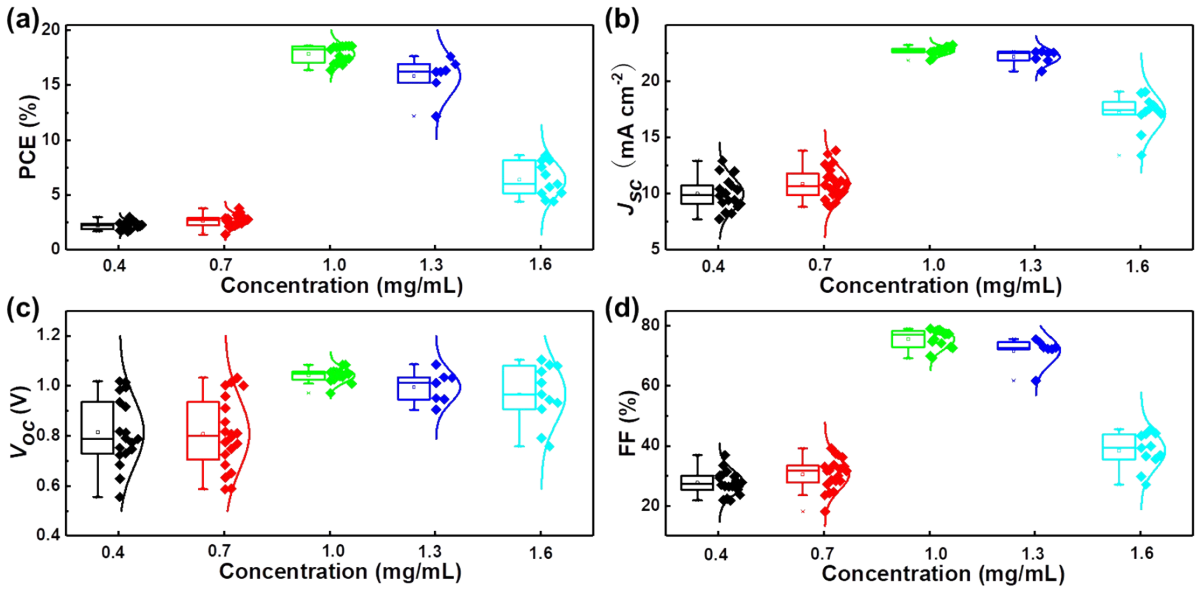

Fig. S17. Box plots of PCE, J_{SC}, V_{OC}, and FF values for solar cells perpared by *in-situ* blended CZ-C4PA under different concentrations.

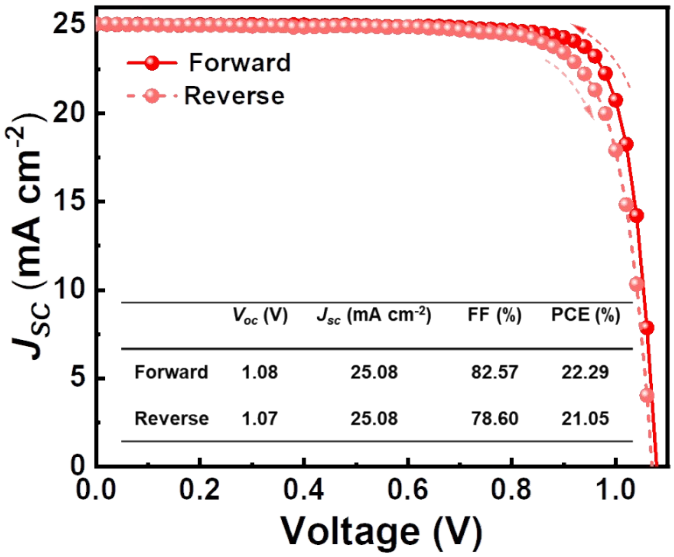

	V_{oc} (V)	J_{sc} (mA cm^{-2})	FF (%)	PCE (%)
Forward	1.08	25.08	82.57	22.29
Reverse	1.07	25.08	78.60	21.05

Fig. S18. Fig. R2. *J-V* responses, in reverse and forward scans, of PSCs (Eg =1.55 eV) using DSA strategy.

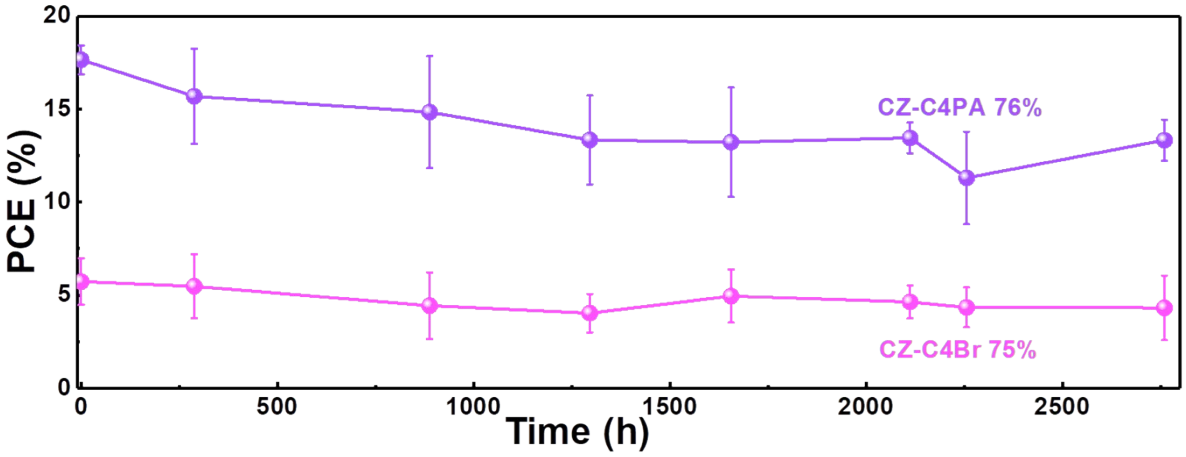

Fig. S19. Stability assessments of uncapsulated PSCs prepared by ISSA strategy using CZ-C4PA and CZ-C4Br.

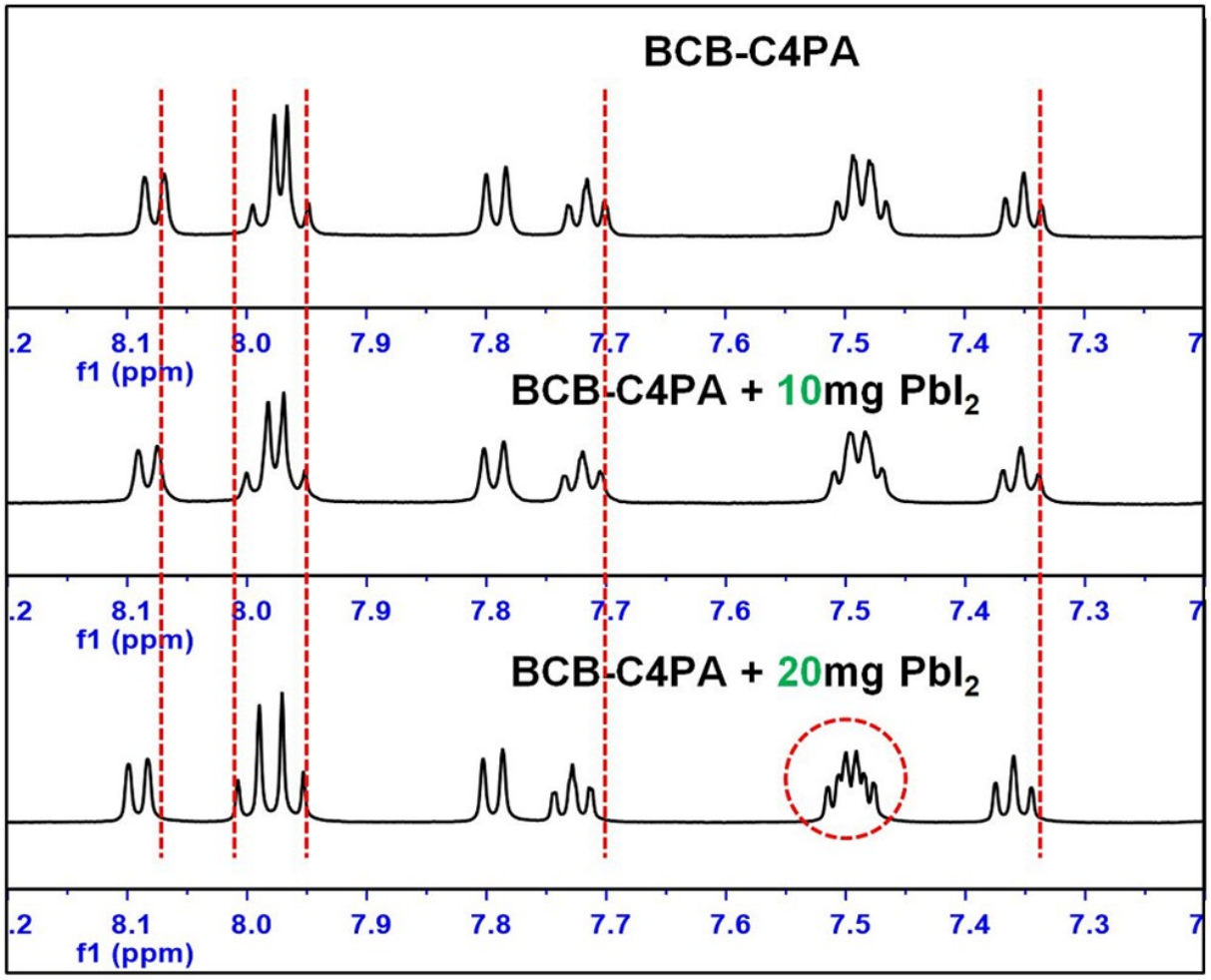

Fig. S20. Comparison of the ^{1}H NMR spectra of BCB-C4PA (in DMSO-d6) with or without mixing with PbI_2. Red dotted lines show down-field shifts of proton peaks after adding PbI_2.

3. Tables

Table S1. The synthesis cost of BCB-C4PA.

Materials	**Dosage (g)**	**Price of Chemical ($/kg)**	**Chemical Cost ($)**	**Target product ($/g)**
BCB-C4Br				
BCB	2.0	7522	15.04	**8.61**
1,4-dibromobutane	40.0	56.5	2.26	
Tetrabuthylammonium bromide	0.59	13.8	0.01	
KOH	2.58	5.5	0.01	
Dichloromethane	245.5	2.1	0.51	
$MgSO_4$	1.3	8.8	0.01	
Silica gel	210.5	7.5	1.58	
petroleum ether	640.5	3.3	1.12	
Expect 3.24g Yield 77%	Product 2.50g		21.53	

BCB-C4P

BCB-C4Br	2.3	8610	19.80	**10.49**
Triethyl phosphite	21.7	58.9	1.28	
Dichloromethane	510.4	2.1	1.07	
ethyl acetate	155.5	2.6	0.40	
Expect 2.67g Yield 80%	Product 2.15g		22.55	

BCB-C4PA

BCB-C4P	2.0	10490	20.98	**19.95**
Bromotrimethylsilane	7.48	133.4	1.00	
1,4-dioxane	14.6	37.2	0.54	
Methanol	12.1	2.1	0.02	
Expect 1.73g Yield 65%	Product 1.13g		22.54	

Table S2. The carrier transport and recombination resistance of devices with *in-situ* blended BCB-C4PA,CZ-C4PA, CZ-C4Br and independently spin-coated BCB-C4PA.

HTL	R_s (Ω)	R_{ct} (Ω)	R_{rec} (Ω)
(sc)BCB-C4PA	18.37	1975	1141
BCB-C4PA	28.99	26.7	1586
CZ-C4PA	20.44	2222	1079
CZ-C4Br	19.63	5655	8979

Table S3. TRPL fitted parameters and the corresponding average lifetimes (τ_{avg}) of CsMAFA films with or without respective HTLs.

HTL	A_1 (μs)	τ_1 (μs)	A_2 (μs)	τ_2 (μs)	τ_{avg} (μs)
(sc)BCB-C4PA	5.35	0.35	94.65	2.91	2.9
BCB-C4PA	5.01	0.09	94.99	2.34	2.3
CZ-C4PA	4.01	0.21	95.99	2.83	2.8
CZ-C4Br	0.03	0.04	99.97	2.94	2.9
Perovskite	0.11	0.007	99.89	3.08	3.1

References

1. A. Al-Ashouri, A. Magomedov, M. Roß, M. Jošt, M. Talaikis, G. Chistiakova, T. Bertram, J. A. Márquez, E. Köhnen, E. Kasparavičius, S. Levcenco, L. Gil-Escrig, C. J. Hages, R.

Schlatmann, B. Rech, T. Malinauskas, T. Unold, C. A. Kaufmann, L. Korte, G. Niaura, V. Getautis, S. Albrecht, *Energy Environ. Sci*., 2019, **12**, 3356-3369.
2. A. Ullah, K. H. Park, H. D. Nguyen, Y. Siddique, S. F. A. Shah, H. Tran, S. Park, S. I. Lee, K. K. Lee, C. H. Han, K. Kim, S. Ahn, I. Jeong, Y. S. Park, S. Hong, *Adv. Energy Mater*., 2022, **12**, 2103175.
3. J. Zhou, X. Yin, Z. Dong, A. Ali, Z. Song, N. Shrestha, S. S. Bista, Q. Bao, R. J. Ellingson, Y. Yan, W. Tang, *Angew Chem. Int. Ed.*, **2019**, *58*, 13717-13721.
4. X. Luo, Z. Shen, Y. Shen, Z. Su, X. Gao, Y. Wang, Q. Han, L. Han, *Adv Mater.*, 2022, **34**, 2202100.
5. K. Wei, L. Yang, J. Deng, Z. Luo, X. Zhang, J. Zhang, *ACS Appl. Energy Mater.*, 2022, **5**, 7458-7465.
6. G. Du, L. Yang, C. Zhang, X. Zhang, N. Rolston, Z. Luo, J. Zhang, *Adv. Energy Mater.*, 2022, **12**, 2103966.